Asteroseismic Diagnostics for Red Giants with Kepler: Measuring ε and Small Frequency Separations in 16,000 Stars

Yingxiang Wang(王颖翔),[1]★ Timothy R. Bedding,[1] Yaguang Li(李亚光),[2] Yifan Chen(陈逸凡),[1] Courtney L. Crawford,[1] Daniel Huber[2] and K. R. Sreenivas[1]
[1]*Sydney Institute for Astronomy (SIfA), School of Physics, University of Sydney, NSW 2006, Australia*
[2]*Institute for Astronomy, University of Hawai'i, 2680 Woodlawn Drive, Honolulu, HI 96822, USA*

Accepted XXX. Received YYY; in original form ZZZ

ABSTRACT

Asteroseismic studies of red giants have primarily relied on two global parameters: the large frequency separation ($\Delta\nu$) and the frequency of maximum power ($\nu_{\rm max}$). Meanwhile, the p-mode phase shift (ε) and small frequency separations ($\delta\nu_{01}$, $\delta\nu_{02}$), which offer additional constraints on stellar interiors, remain underexplored due to measurement challenges. We present an automated method using collapsed échelle diagrams to measure these parameters from *Kepler* light curves of ∼16,000 red giants, creating the largest homogeneous catalogue to date. We also update $\Delta\nu$ values. The small separations show distinct evolutionary signatures: $\delta\nu_{02}/\Delta\nu$ stays nearly constant for RGB stars but splits into two groups for CHeB stars, separating the red clump and secondary clump populations and confirming the dependence of the helium flash limit on metallicity. Comparisons with stellar models corroborate these findings. Our results for $\delta\nu_{01}$ and ε, combined with a new grid of theoretical models, enable surface corrections to be applied to red clump stars. Overall, this work demonstrates that ε and the small separations, although previously underappreciated in red giant seismology, provide critical diagnostics of stellar structure and evolution that are complementary to those provided by $\Delta\nu$ and $\nu_{\rm max}$ alone.

Key words: stars: oscillations – stars: evolution – stars: solar-type

1 INTRODUCTION

Asteroseismic analysis of red giants provides critical insights into stellar evolution through the detection of oscillations. Recent surveys by the space missions such as *CoRoT* (Baglin et al. 2006), *Kepler* (Borucki et al. 2008), and *TESS* (Ricker et al. 2015) have enabled systematic studies of these oscillations (see reviews by Chaplin & Miglio 2013; Jackiewicz 2021). While asteroseismic techniques can, in principle, use full sets of stellar oscillation frequencies, population-scale analyses often rely on two key global parameters: the large frequency separation ($\Delta\nu$), and the frequency of maximum oscillation power ($\nu_{\rm max}$). These parameters have yielded precise mass and radius determinations for over 16,000 red giants in *Kepler* Data Release 25 (DR25) (Mosser et al. 2010; Yu et al. 2018; Hon et al. 2024; Pinsonneault et al. 2025).

However, additional seismic parameters such as the small frequency separations ($\delta\nu_{0l}$) and the phase shift (ε) have been mostly neglected in red giants asteroseismology. These parameters are defined by the asymptotic relation for acoustic modes (Tassoul 1980):

$$\nu_{n,l} \approx \Delta\nu \left(n + \frac{l}{2} + \varepsilon\right) - \delta\nu_{0l}, \tag{1}$$

where n denotes the radial order, l is the spherical degree, and $\delta\nu_{0l}$ represents spacings between non-radial ($l \neq 0$) and radial ($l = 0$) p-modes. In observations, there are two small separations that can be estimated in a large number of solar-like oscillators: $\delta\nu_{02}$ and $\delta\nu_{01}$. To be explicit, for a given radial order, n, these separations are defined as follows:

$$\delta\nu_{02} = \nu_{n,l=0} - \nu_{n-1,l=2} \tag{2a}$$

$$\delta\nu_{01} = \frac{1}{2}(\nu_{n,l=0} + \nu_{n+1,l=0}) - \nu_{n,l=1} \tag{2b}$$

For main-sequence stars, these parameters are established as direct diagnostics of interior structure, and depend on masses and ages of solar-like oscillators (e.g. Roxburgh & Vorontsov 2003; Roxburgh 2005; Otí Floranes et al. 2005). Such an interpretation is based on a well-known integral estimator relating $\delta\nu_{02}$ to a radially averaged sound-speed gradient. However, for red giants, the small separations are much less sensitive to their internal structure (Montalbán et al. 2010; Christensen-Dalsgaard 2014).

Recently, ε and $\delta\nu_{02}$ have been reported to help constrain the properties of convective boundary mixing, especially when undershooting occurs below the convective envelope (Ong et al. 2025; Reyes et al. 2025). However, for red giants, systematic measurements of $\delta\nu_{01}$ and $\delta\nu_{02}$ still remain confined to small samples (Huber et al. 2010; Corsaro et al. 2012). This reveals potential to expand high-precision $\delta\nu_{01}$, $\delta\nu_{02}$ and ε measurements to larger samples, strengthening connections between stellar models and observations. Complementary *TESS* results with individual frequencies and asymptotic parameters for red giants have recently been presented by Zhou et al. (2025),

★ E-mail: ywan0509@uni.sydney.edu.au

© 2025 The Authors

providing an ensemble view that complements our Kepler-based catalogue.

This work aims to extend high-precision determinations of $\delta\nu_{01}$, $\delta\nu_{02}$ and ε to all $\sim$ 16,000 *Kepler* red giants, and to refine $\Delta\nu$ for the same sample, thereby improving mass estimates via the seismic scaling relations. By analysing these parameters across evolutionary phases, we investigate their correlations with fundamental stellar properties and test theoretical models linking seismic observables to internal structure. Our results demonstrate that small separations and phase shifts, although historically neglected in red giants, offer critical constraints on stellar evolution not accessible through $\Delta\nu$ and $\nu_{\rm max}$ alone. Using collapsed échelle diagrams, we measure phase shifts (ε) and small frequency separations ($\delta\nu_{01}$, $\delta\nu_{02}$) for $\sim$ 20,000 *Kepler* red giants in Section 2. At the same time, we also produce more accurate measurements of $\Delta\nu$. Section 3 presents our seismic catalogue. In Section 4, we compare observations with models. Finally, Section 5 summarizes our findings and their implications.

2 METHODOLOGY

The method we used to estimate $\Delta\nu$, ε, $\delta\nu_{02}$, and $\delta\nu_{01}$ can be summarized in the following steps:

(i) **Prepare the oscillation spectrum**: Remove background noise and adjust extreme peaks to ensure balanced mode amplitudes (Section 2.1).
(ii) **Create the collapsed échelle diagram**: Fold the processed spectrum at $\Delta\nu$ intervals (Section 2.2).
(iii) **Optimise the large frequency separation**: Sample trial values of $\Delta\nu$ and select the one that maximises ridge prominence in the collapsed diagram, ensuring consistent global structure (Section 2.3).
(iv) **Extract the seismic parameters**: Perform constrained fitting of ridge centroids and widths to measure ε, $\delta\nu_{02}$, and $\delta\nu_{01}$ from the optimised collapsed diagram (Section 2.4).

2.1 Preparation of Oscillation Spectrum

To prepare the oscillation spectrum for analysis, we started from power spectra computed from *Kepler* long-cadence light curves, prepared as described in Section 3.1. No additional time-domain detrending beyond that pipeline was applied at this stage. We then made two adjustments to the raw power spectrum:

2.1.1 Isolating the region of oscillation power

Noise outside the oscillation region biases the collapsed échelle diagram: after folding the spectrum modulo $\Delta\nu$ and averaging across orders, out-of-envelope power elevates the baseline and can introduce spurious local maxima, which pull the centroid of the collapsed profile and hence bias ε (and inflate its uncertainty). To mitigate this, we multiply the power spectrum by an order-4 super-Gaussian window centred at $\nu_{\rm max}$:

$$W(\nu) = \exp\left(-\left[\frac{\nu-\nu_{\rm max}}{\left(\frac{3\times0.66}{2.355}\right)\nu_{\rm max}{}^{0.88}}\right]^4\right). \quad (3)$$

An example is shown in Figure 1(a). Here the window width is tied to the oscillation-power envelope in red giants, which is well described by a Gaussian with full width at half maximum (FWHM) $\delta\nu_{\rm env} = 0.66\,\nu_{\rm max}{}^{0.88}$ (Mosser et al. 2012). We convert the FWHM to a Gaussian dispersion via $\sigma \equiv \delta\nu_{\rm env}/2.355$, and adopt a half-width of 3σ in the super-Gaussian so that power within the envelope is preserved while out-of-envelope background is sharply attenuated. As the figure illustrates, the super-Gaussian leaves the power near $\nu_{\rm max}$ essentially unchanged but rapidly suppresses distant frequencies, stabilizing the collapsed profile and the ε estimate.

2.1.2 Peak Adjustment

In red giants, convection stochastically excites and damps oscillation modes (Houdek et al. 1999; Samadi & Goupil 2001), causing amplitude variations. Because of this, some modes occasionally show unusually strong peaks, which can distort measurements in collapsed échelle diagrams (especially ε values) because they disproportionately affect averaged positions. To prevent this distortion, we identified peaks with amplitudes significantly higher than other modes using a median absolute deviation (MAD) rule: a peak of height h_i was flagged when $h_i > \tilde{h} + \kappa\,\mathrm{MAD}$, where $\tilde{h}$ is the sample median across detected peaks and MAD is the median absolute deviation; we used $\kappa = 5$. For each unusual peak, we reduced its amplitude to match the strongest neighbouring peak within a symmetric window whose half-width equals c times the peak's FWHM, leaving the frequency unchanged.

2.2 Collapsed Échelle Diagram

From the prepared oscillation spectrum, we extract global asteroseismic parameters using a collapsed échelle diagram. Conceptually, this extends traditional échelle analysis (Grec et al. 1983) by folding the power spectrum modulo the large frequency separation, $\Delta\nu$, and summing vertically to form a one-dimensional collapsed profile (see Fig. 1b,d). The collapsed idea was already introduced for solar data by Grec et al. (1983) and for solar-like stars (e.g. Bouchy & Carrier 2002; Bedding et al. 2004), and a related folded-spectrum method has been used in automated pipelines; see Zinn et al. (2019) for a K2 application. Before folding, we applied two pre-processing steps to improve the visibility of the ridge pattern while preserving frequency separations. As in Section 2.1.1, we applied the same super-Gaussian window centred on $\nu_{\rm max}$ to down-weight power far from the oscillation hump. This suppresses granulation/shot-noise outside the envelope. Second, we performed a Gaussian smoothing with a FWHM of $0.03\,\Delta\nu$ to reduce pixel-to-pixel variance without biasing the relative ridge phases.

The folding process combines power from modes separated by integer multiples of $\Delta\nu$. In the collapsed échelle, each angular-degree ridge ($l = 0, 1, 2$) therefore appears as a *phase-aligned aggregate peak* at its characteristic phase. These peaks correspond to ridge structures in standard échelle diagrams [Fig. 1(b)] but reduced to one dimension [Fig. 1(d)]. By focusing on the overall ridge pattern rather than individual mode peaks, the collapsed representation enables robust mode identification and efficient measurement of $\delta\nu_{02}$, $\delta\nu_{01}$, and ε via spectrum stacking and constrained least-squares fitting (see Section 2.3 for the trial-$\Delta\nu$ scan and scoring). To mitigate edge effects, we duplicate the échelle pattern by one radial order prior to collapsing (Bedding 2012).

2.3 Refining the Large Frequency Separation ($\Delta\nu$)

An accurate initial estimate of the large frequency separation, $\Delta\nu_0$—initialised as described in Section 3.1—is essential because it sets the folding interval of the collapsed échelle diagram and directly

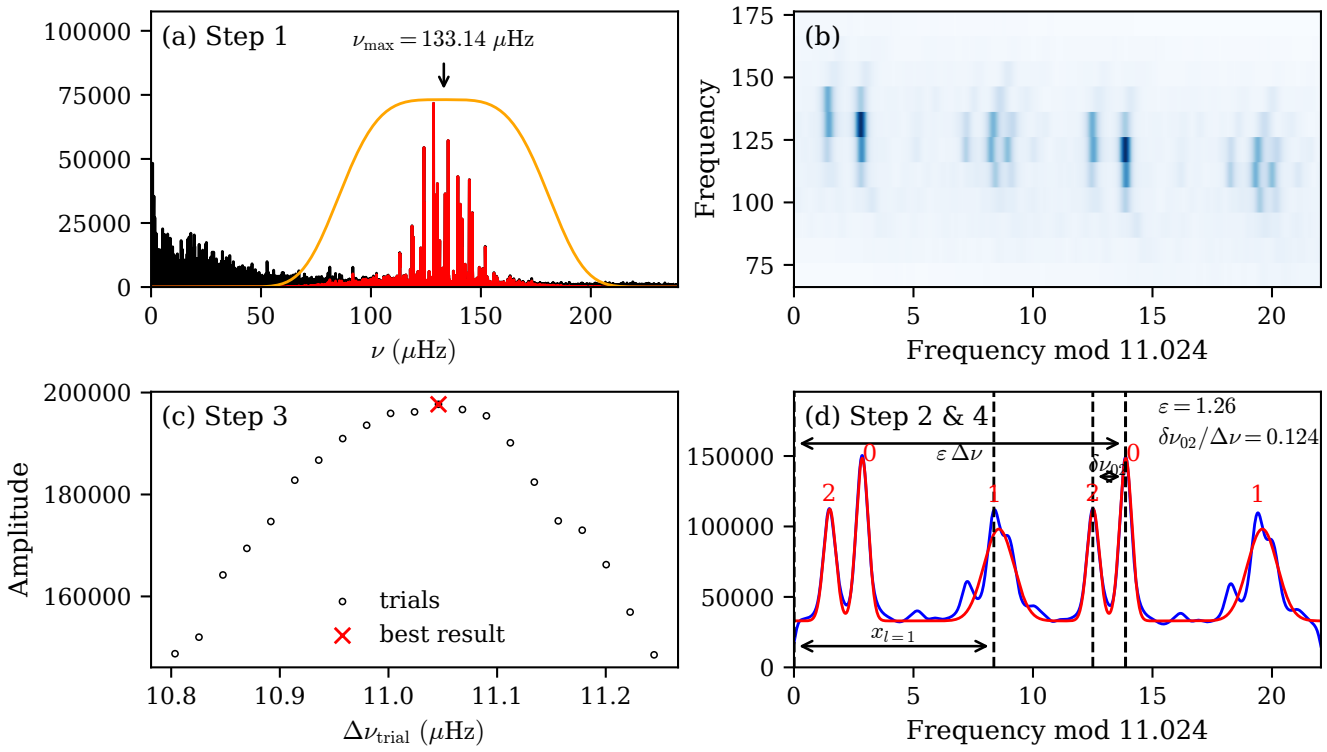

Figure 1. Illustration of collapsed échelle diagram for star KIC 3530333. The upper panel shows power spectrum. The lower panels show the échelle and collapsed diagrams with $\Delta\nu = 10.95\mu$Hz. The red numbers represent the angular degree l of oscillation modes.

affects the reliability of all subsequent parameter measurements. To refine $\Delta\nu$, we performed a systematic sampling around the initial value, using an interval of ±8% to account for potential systematic deviations. This results in a trial range defined by

$$\Delta\nu_{\rm trial} \in [0.92\Delta\nu_0,\ 1.08\Delta\nu_0]\,. \tag{4}$$

For each trial $\Delta\nu_{\rm trial}$, we constructed the collapsed échelle diagram using the pre-processed spectrum described in Section 2.2 and fitted a three-ridge parametric model ($l = 0, 1, 2$) plus a constant background while keeping $\Delta\nu_{\rm trial}$ fixed. The model includes ridge phases (parameterised by ϵ for $l = 0$, the dipole position x_1, and the quadrupole offset $\delta\nu_{02}$), amplitudes (A_0, A_1, A_2), and linewidths $(\Gamma_0, \Gamma_1, \Gamma_2)$, together with a background level B. Parameters were estimated by minimising square-root–weighted residuals between model and data, $(\text{model} - \text{data})/\sqrt{P_{\rm coll} + 10^{-6}}$, using the derivative-free Nelder–Mead algorithm as implemented in `lmfit` (Newville et al. 2025).

As a scalar measure of ridge clarity we adopted a ridge-contrast score,

$$\mathcal{R} \equiv A_0 + A_2,$$

and selected the $\Delta\nu_{\rm trial}$ that maximised $\mathcal{R}$. The small separation between the radial and quadrupole ridges was required to satisfy

$$0.07\,\Delta\nu \le \delta\nu_{02} \le 0.22\,\Delta\nu, \tag{5}$$

consistent with previous studies (Huber et al. 2010). When the quadrupole signature was weak ($A_2 < 0.1\,A_0$), we applied a fallback solution using only the radial ridge, which preserves robustness in stars with suppressed quadrupole modes (Stello et al. 2016a).

2.4 Precise Parameter Extraction

With the optimal $\Delta\nu$ determined in Section 2.3, we refitted the *same* three-ridge model ($l = 0, 1, 2$) to the collapsed échelle diagram, now with $\Delta\nu$ fixed at its optimum. This final fit returns ridge centroids, amplitudes, linewidths, and background, from which we derived the phase shift ε and the small frequency separations $\delta\nu_{02}$ and $\delta\nu_{01}$ (see panel (d) of Fig. 1). To guard against misidentification and overfitting, we enforced the empirical constraint in Eq. (5). If the optimised $\delta\nu_{02}$ approached either boundary, or if the quadrupole amplitude was negligible ($A_{l=2} < 0.1\,A_{l=0}$), a fallback model assuming a single $l = 0$ ridge was applied.

The dipole-mode small separation was computed from the fitted centroids as

$$\delta\nu_{01} = \begin{cases} \dfrac{\Delta\nu}{2} - (x_{l=1} - x_{l=0}), & x_{l=1} \ge x_{l=0}, \\ -\dfrac{\Delta\nu}{2} - (x_{l=1} - x_{l=0}), & \text{otherwise.} \end{cases} \tag{6}$$

No additional empirical scaling relations (e.g. amplitude ratios or temperature-dependent linewidth trends) were applied at this stage. The final parameters thus follow directly from the constrained fitting and provide an internally consistent solution based on the observed ridge structure in the collapsed diagram.

3 SAMPLE SELECTION AND SEISMIC PARAMETER EXTRACTION

3.1 Data and Sample Selection

We used *Kepler* long-cadence photometry covering Quarters Q0–Q17, which provides a nearly continuous 44-month observational baseline. As our sample, we adopted the catalogue of oscillating red giants compiled by Yu et al. (2018), comprising 16,094 stars identified from the full four-year dataset. We excluded the additional targets reported by Hon et al. (2019) that are not in Yu et al. (2018) because, for many of those stars, only $\nu_{\max}$ can be measured robustly from the available light curves. Our analysis and statistics therefore refer exclusively to the Yu et al. (2018) sample.

For all stars in this initial sample, we retrieved the full 4-year set of Pre-search Data Conditioning Simple Aperture Photometry (PDC-SAP) light curves (Smith et al. 2012; Stumpe et al. 2012). Following the methodology outlined in Section 2 of Sreenivas et al. (2024), we processed the light curves to calculate the power spectra. This nuSYD pipeline includes steps for instrumental correction and granulation noise removal, enabling robust extraction of global seismic parameters. As part of this procedure, we also remeasured the frequency of the maximum oscillation power, $\nu_{\max}$, for each target.

To initialise the large frequency separation, $\Delta\nu_0$, we used the $\Delta\nu$ values reported by Yu et al. (2018) wherever available (i.e., for all stars in our sample). As a cross-check, we also tested initialisation from the empirical $\nu_{\max}$–$\Delta\nu$ relation,:

$$\Delta\nu_0 = \alpha \cdot (\nu_{\max})^{\beta},$$

with $\alpha = 0.267 \pm 0.002$ and $\beta = 0.764 \pm 0.002$, as calibrated in Yu et al. (2018) (see their Section 3.6). In practice, the optimisation described in Section 3.1 converged to the same $\Delta\nu$ (within our quoted uncertainties) whether initialised from literature values or from the empirical relation. This robustness reflects the broad (±8%) trial neighbourhood around the initial guess and the fact that the windowing in Section 3.1 acts on scales much larger than $\Delta\nu$ and thus does not shift ridge phases.

After combining the available data and applying our quality filters, we defined a final working set drawn exclusively from the Yu et al. (2018) *Kepler* red-giant sample. Evolutionary states (RGB vs. core-helium-burning) were assigned by cross-matching Vrard et al. (2025) to our star list; their catalogue combines six independent seismic diagnostics and reports labels for 18,784 *Kepler* red giants. For stars in our sample without a label in Vrard et al. (2025), we adopted the classification reported by Yu et al. (2018); objects lacking a label in both sources were left unclassified.

3.2 Measurements and Overall Statistics

We determined $\Delta\nu$, $\delta\nu_{02}$, $\delta\nu_{01}$, and ε for 16,050, 15,279, 15,400, and 15,602 red giants, respectively. The results are shown in Figure 2 and all measured parameters are listed in Table 1. The absence of measured values in some stars can be attributed to several factors. First, we did not report a value from when the fit was unstable or the mode identification was uncertain. We flagged a fit as unstable if the optimiser failed to converge or returned a non–positive-definite covariance matrix. We flagged the mode identification as uncertain when the collapsed échelle ridge contrast fell below a fixed threshold or when multiple competing maxima of comparable height were present; the formal criteria are given in Section 2.3. Second, data-related issues, such as poor data quality, insufficient observation durations, or excessive noise, can hinder the detection of the oscillation modes. Finally, astrophysical factors, such as mode suppression,

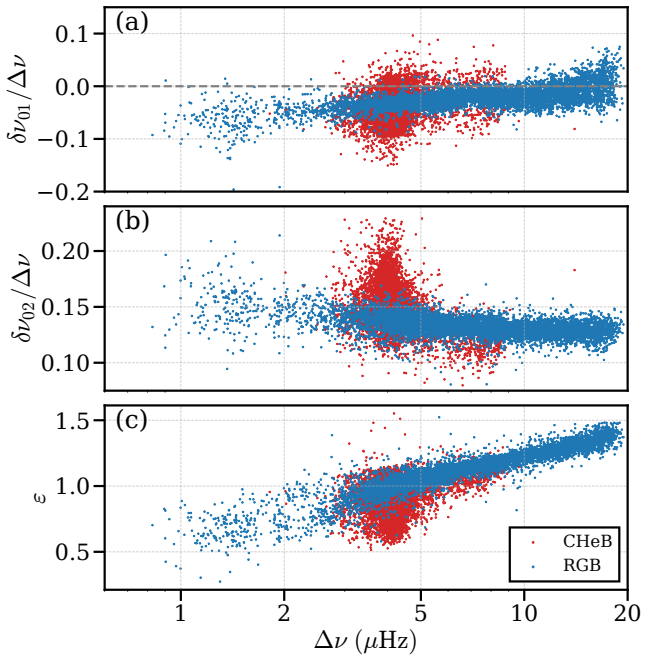

Figure 2. Frequency separation ratio diagrams of $\delta\nu_{0l}/\Delta\nu$ for $l = 1$, and $l = 2$ and ε diagram. Blue and red points represent RGB and CHeB stars, respectively.

strong magnetic activity/fields, rapid rotation, or mixed-mode crowding, may also play a role, especially in stars that differ significantly from the majority of our sample and might require distinct treatment in terms of mode identification. For example, mode suppression can cause the $l = 1$ and $l = 2$ modes of oscillation to be absent in some stars (Stello et al. 2016b). These limitations may lead to the absence of measurements or misidentifications in some stars.

We estimated uncertainties by generating 200 Monte Carlo realizations per star, perturbing each power-density spectrum with a χ^2 distribution with two degrees of freedom, and repeating the full fit; the standard deviation of the posterior samples was adopted as the 1σ uncertainty (Huber et al. 2011). In Table 1, we report the absolute 1σ uncertainties for the measured quantities. The typical (median) uncertainties are ∼0.57% in $\Delta\nu$, ∼0.0036 in r_{01}, ∼0.0015 in r_{02}, and ∼0.62% in ε; stars with time series longer than 1200 days show slightly smaller values, but the overall distributions are similar. For these summary statistics, we quote fractional precision for $\Delta\nu$ and ε, and the uncertainties of the dimensionless ratios $r_{01} \equiv \delta\nu_{01}/\Delta\nu$ and $r_{02} \equiv \delta\nu_{02}/\Delta\nu$ (rather than $\sigma/|\delta\nu_{0l}|$), which avoids ill-defined values when $\delta\nu_{01}$ crosses or approaches zero.

3.2.1 *C–D Diagrams and Evolutionary Trends*

Figure 2(b) shows the results in a modified version of the so-called C–D diagram (Christensen-Dalsgaard 1988), which plots the ratio $\delta\nu_{02}/\Delta\nu$ versus $\Delta\nu$. A similar C–D diagram for *Kepler* red giants was shown by Miglio et al. (2021, their Fig. A.3), which provides a recent ensemble view of the RGB and RC sequences consistent with our layout. The small separation, $\delta\nu_{02}$, measures the frequency difference between two modes with nearly identical eigenfunction shapes in the outer layers of the star. This separation is sensitive to changes in the slope of the sound speed in the star's deep interior, making it a useful diagnostic for stellar evolution. For stars on

Table 1. Catalogue of measurements for 16,050 red giants. Only the first ten rows are shown. The complete machine-readable table is archived on Zenodo (DOI: 10.5281/zenodo.17225960; the DOI will be activated upon publication).. Uncertainties in parentheses denote 1σ.

KIC	$\Delta\nu$ (μHz)	$\delta\nu_{01}$ (μHz)	$\delta\nu_{02}$ (μHz)	ε
757137	3.406(0.012)	−0.136(0.018)	0.444(0.018)	0.900(0.0060)
892010	2.451(0.007)	−0.113(0.012)	0.383(0.613)	0.784(0.0046)
892738	1.221(0.002)	−0.119(0.305)	0.215(0.305)	0.958(0.250)
893214	4.302(0.020)	−0.112(0.016)	0.572(0.012)	1.008(0.0054)
1026084	4.458(0.073)	−0.015(0.036)	0.535(0.001)	0.950(0.015)
1026180	3.967(0.036)	−0.198(0.046)	0.629(0.009)	0.754(0.0070)
1026309	1.931(0.020)	−0.089(0.012)	0.216(0.009)	0.849(0.0093)
1026326	8.848(0.112)	−0.152(0.056)	1.167(0.002)	1.172(0.015)
1026452	4.023(0.020)	−0.037(0.010)	0.668(0.002)	0.855(0.0044)
1027110	1.117(0.001)	−0.113(0.009)	0.194(0.009)	0.824(0.0079)

the main sequence, it tracks the gradual synthesis of a helium core, with $\delta\nu_{02}$ serving as an age indicator (White et al. 2011). However, this method becomes less reliable during the sub-giant phase when the core undergoes minimal evolutionary changes. On the giant branch, the core becomes more centrally concentrated, allowing $\delta\nu_{02}$ to again serve as a measure of stellar evolution, reflecting the state of the hydrogen-burning shell. The cores of RGB and RC stars differ slightly and, as a result, they will show differences in their seismic parameters. As shown in Figure 2(b), we observe that $\delta\nu_{02}$ is almost a fixed fraction of $\Delta\nu$ for RGB stars, which is consistent with previous findings by Bedding et al. (2010) and Huber et al. (2010). During RGB evolution, $\delta\nu_{02}$ increases continuously, whereas CHeB stars exhibit more complex variations. This will be discussed in more detail in Section 4.3.

We observed a larger spread in $\delta\nu_{02}$ for stars with $\Delta\nu < 3\mu$Hz than for stars with higher $\Delta\nu$. This is primarily due to the greater uncertainty in determining $\delta\nu_{02}$: for stars with low $\Delta\nu$, only two or three orders are detectable, significantly reducing the precision of $\delta\nu_{02}$ measurements.

Figure 2(a) shows that $\delta\nu_{01}$ is negative for most red giants, confirming the findings by Bedding et al. (2010). Similarly to the trend observed for $\delta\nu_{02}/\Delta\nu$, we observe a trend (but with opposite sign) in the frequency separation ratio $\delta\nu_{01}/\Delta\nu$ with $\Delta\nu$. The decrease of $\delta\nu_{01}/\Delta\nu$ and the increase of $\delta\nu_{02}/\Delta\nu$ appear to affect stars in the same range of $\Delta\nu$.

3.2.2 The ε–$\Delta\nu$ Relation

Figure 2(c) shows our results for ε, revealing a single $\Delta\nu$–ε relation for all stars, which contrasts with previous reports that showed systematic offsets between RGB and CHeB stars (Bedding et al. 2010; Corsaro et al. 2012; Kallinger et al. 2012). Our best-fitting power-law relation is given by:

$$\varepsilon = (0.610 \pm 0.002) + (0.625 \pm 0.002)\,\log_{10}(\Delta\nu/\mu\text{Hz}) \quad (7)$$

The difference between our results and those of previous studies arises from how the phase offset ε is defined and measured. In the asymptotic relation for radial modes, $\nu_{n0} \simeq \Delta\nu\,(n+\varepsilon)$, the phase ε is in fact a slowly frequency–dependent function perturbed by curvature from acoustic glitches. Two observational estimators are commonly used: (i) A local, "central" estimator ε_c is obtained around $\nu_{\max}$ by defining the central large separation from the two adjacent radial orders and setting $\varepsilon_c = \nu_{n_c,0}/\Delta\nu_c \bmod 1$. This is the quantity used by Kallinger et al. (2012) and formalized in Christensen-Dalsgaard et al. (2014). (ii) A more global, "asymptotic" estimator ε_a is the intercept from a least-squares fit of $\nu_{n,0}$ versus n over a broader window, which averages over local modulations (White et al. 2011; Ong & Basu 2019). Because ε_c is local to $\nu_{\max}$, it is particularly susceptible to the oscillatory contributions from the He II acoustic glitch and ridge curvature, and indeed separates RGB and CHeB stars at fixed $\Delta\nu$ owing to differences in the thermodynamic state of their convective envelopes (Christensen-Dalsgaard et al. 2014). Earlier work, such as Kallinger et al. (2012), effectively measured ε_c because only three radial orders near $\nu_{\max}$ were used, making the measurement particularly sensitive to the He II glitch (Vrard et al. 2015). These glitches cause modulations in the oscillation frequencies that arise from the interaction of sound waves with the steep gradient in the helium ionization zone. Our analysis, on the other hand, uses five or more radial orders, thereby averaging over these glitch-induced perturbations (as shown in Fig. 9 of Vrard et al. 2015). This approach recovers a more consistent ε–$\Delta\nu$ correlation because ε_a is less sensitive to these local effects. See Ong & Basu (2019) for a discussion of these estimators and their systematics.

The presence of acoustic glitches is particularly important for distinguishing between RGB and CHeB stars. In CHeB stars, radial modes often exhibit a characteristic "C-shape" pattern in the échelle diagram (as shown in Figure 1(b)), indicating a deviation from the ideal asymptotic relation in which ridges are perfectly vertical (Mosser et al. 2013; Vrard et al. 2015) . This pattern, interpreted as a glitch signature, means that the observed mode frequencies systematically deviate from uniform spacing. Typically, $\nu_{\max}$ lies in the upper part of the "C-shape"—where the ridge tilts to the right—leading to an overestimation of $\Delta\nu$ when computed from the three central radial modes. As a result, the corresponding ε value is underestimated, which causes a systematic offset in the ε–$\Delta\nu$ relation between RGB and CHeB stars. In contrast, by incorporating a broader range of radial orders, our method mitigates the influence of such glitches and provides a more robust ε–$\Delta\nu$ scaling for all stellar populations.

3.3 Comparison with Existing Catalogues

Figure 3 compares the $\Delta\nu$ values obtained in this work with those from Yu et al. (2018) (upper panel), and with 10,079 stars that overlap with the APOKASC-3 catalogue (Pinsonneault et al. 2025) (lower panel), spanning a broad range of evolutionary states. Across the full interval of $\Delta\nu \in [1,\ 20]\,\mu$Hz, our measurements show excellent consistency with APOKASC-3, indicating the robustness of our pipeline. However, compared to the SYD pipeline results from Yu et al. (2018), we observe an oscillatory structure in the residuals for stars with $\Delta\nu > 11\,\mu$Hz. This pattern reflects a subtle systematic error in SYD measurements. Despite this, over 99% of the RGB sample lies within a 1% deviation, indicating strong overall agreement.

For core helium-burning (HeB) stars (red points in Figure 3), a small systematic offset is evident relative to both APOKASC-3 and Yu et al. (2018). This discrepancy primarily arises from oscillation glitches that are characteristic of the HeB phase (Vrard et al. 2015). Our clipping approach (Section 2.1), which attenuates anomalously strong peaks, tends to yield slightly lower $\Delta\nu$ values and correspondingly higher ε estimates. A discussion of how glitch structures and peak clipping affect the inference of $\Delta\nu$ and ε is presented in Section 3.2.2.

As an external check, we cross-matched our catalogue with the APOKASC peak-bagging release by Kallinger (2019), and compared the quadrupole small separation on a star-by-star basis. We found no evidence for a systematic offset in $\delta\nu_{02}$ between the two catalogues;

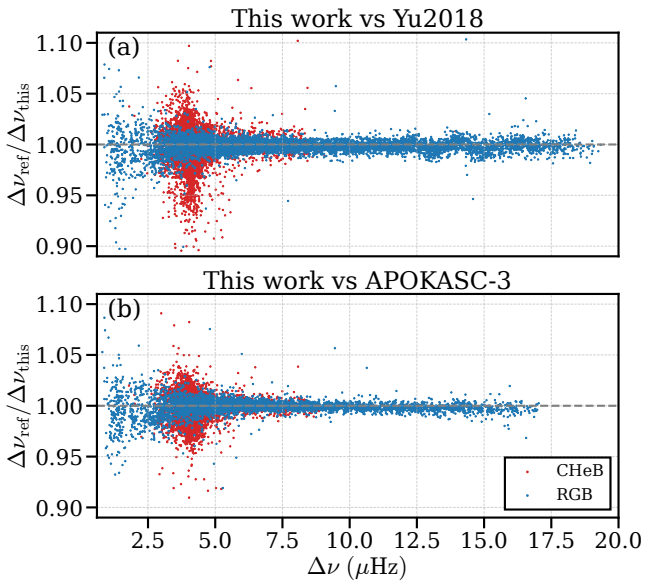

Figure 3. Comparison of $\Delta\nu$ values derived in this work with those from Yu et al. (2018) and Pinsonneault et al. (2025). (a) the relative differences $(\Delta\nu_{\rm Yu18} - \Delta\nu_{\rm this\ work})/\Delta\nu_{\rm this\ work}$, with RGB stars in blue and CHeB stars in red. (b) the relative differences $\Delta\nu_{\rm APOKASC\text{-}3} - \Delta\nu_{\rm this\ work}$.

the relative differences are small and consistent with our uncertainties on r_{02}. This agreement supports the validity of the collapsed-échelle measurements adopted here. A direct comparison of ε is not presented because the Kallinger release provides central three-order quantities tied to local definitions, whereas our work reports a global (asymptotic) estimator; mixing these two conventions would not constitute a like-for-like test (see discussion in Section 3.2.2).

4 COMPARISON WITH MODELS

4.1 Stellar Models

To compare our results with theoretical predictions, we computed a set of stellar evolutionary models using MESA (r24.03.1 Paxton et al. 2011, 2013, 2015, 2018, 2019; Jermyn et al. 2023) and GYRE (v7.1 Townsend & Teitler 2013) implemented within `run_star_extras` (GYRE on-the-fly; Bellinger & Christensen-Dalsgaard 2022; Joyce et al. 2024). Evolutionary tracks were calculated for stellar masses ranging from 0.6 to 3.6 $M_\odot$ in steps of 0.2 $M_\odot$, and for initial metallicities from −1.2 to 0.4 dex in steps of 0.4 dex. The initial helium abundance varied with metal abundance linearly according to the relation $Y_{\rm init} = 0.249 + 1.5 Z_{\rm init}$ (Planck Collaboration et al. 2016; Choi et al. 2016). The solar abundance scale follows Asplund et al. (2009), with $Z_\odot = 0.0134$ and $X_\odot = 0.7381$. The mixing length parameter was fixed at 2.2. The convective core overshoot was modelled as a function of stellar mass, using the fitting relation from Claret & Torres (2019). Other mixing processes, including convective shell overshoot, semiconvection, and thermohaline mixing, were set according to the MIST isochrone settings (Choi et al. 2016). The full MESA working directory, including inlist files and other custom settings used to generate these models, is publicly available on Zenodo (reserved DOI: 10.5281/zenodo.17226468)..

For each model, we computed oscillation frequencies for modes with spherical degrees $0 \leq l \leq 2$ in the frequency range around $\nu_{\rm max}$. For non-radial modes, we included solutions from both the full set of oscillation equations, which yield mixed modes (Townsend & Teitler 2013), and the reduced set in the $\omega^2 \gg N^2$ limit (ω is the angular frequency and N is the buoyancy frequency). The latter allows computation of π modes, which are pure p modes in the absence of g-mode coupling (Ong & Basu 2020).

To place the models on the same footing as the observations, each MESA+GYRE snapshot was converted into a synthetic power–density spectrum (PDS) centred on $\nu_{\rm max}$. We placed a Lorentzian at every $l = 0, 1, 2$ mode frequency, modulated by a Gaussian envelope $\propto \exp[-(\nu - \nu_{\rm max})^2/(2\sigma^2)]$ with $\sigma = 0.66\,{\nu_{\rm max}}^{0.888}/2.355$ (Mosser et al. 2012), and adopted fixed relative mode visibilities of $A_{l=0} : A_{l=1} : A_{l=2} = 1 : 0.8 : 0.6$. Line widths were prescribed as simple functions of $\Delta\nu$ and evolutionary state (RGB vs. CHeB). The PDS was lightly smoothed and collapsed into an échelle spectrum using exactly the same settings as for the observations.

We measured $\Delta\nu$, ε, $\delta\nu_{01}$, and $\delta\nu_{02}$ from each synthetic PDS using the same pipeline as for the observations. For direct comparison we also report the dimensionless ratios $r_{01} \equiv \delta\nu_{01}/\Delta\nu$ and $r_{02} \equiv \delta\nu_{02}/\Delta\nu$. We present three figures (Figure 4–6) that each contain four panels: the upper row corresponds to the RGB stars and the lower row to the CHeB stars. Each row includes observational data (left) and pure p-mode (π-mode) model predictions (right), colour-coded by mass. In the right panels, the observed values are shown as grey points in the backgroud. In each figure, the x-axis represents $\Delta\nu$, while the y-axis represents one of the seismic parameters. The model points shown were measured on the synthetic PDS using the procedure above, ensuring that $\Delta\nu$, $\delta\nu_{01}$, $\delta\nu_{02}$, and ε are defined identically for models and observations.

4.2 ε & $\delta\nu_{01}$: Surface Corrections

Figure 4 compares the observed ε values with those predicted by stellar models. A systematic deviation is evident across both RGB and CHeB stars, indicating the presence of surface effects—that is, the well-known offsets between observed and modelled oscillation frequencies caused by imperfect physics in the outermost stellar layers (e.g. turbulent convection, atmospheric boundary conditions, and non-adiabaticity). The linear relationship between ε and $\Delta\nu$ (Equation 7) shows an offset between models and observations, which is consistent with the findings of White et al. (2011), and this difference arises because current stellar models are inaccurate near the surface. Notably, the difference is consistent between RGB and CHeB stars, implying that a single surface correction prescription may apply to both evolutionary phases.

This result can be combined with the findings of Li et al. (2023), who derived a surface correction formula for RGB stars based on surface gravity, effective temperature, and metallicity. Our data suggest that their prescription can be extended to CHeB stars, given the similar systematic offsets in ε observed in both evolutionary phases. This compatibility further supports the potential for a unified surface correction framework applicable to evolved stars.

Figure 5 shows clear differences between the observed and modelled $\delta\nu_{01}$ values, especially for RGB stars, whereas the measured $\delta\nu_{01}$ for CHeB stars shows a wide spread. This is likely because their high coupling strength makes $l = 1$ mixed modes difficult to identify (Dhanpal et al. 2023). This structural complexity adds uncertainty to $\delta\nu_{01}$ measurements.

The presence of systematic offsets in both ε and $\delta\nu_{01}$ provides important insights into the nature of surface effects. If surface corrections were applied uniformly to both $l = 1$ and $l = 0$ modes following the prescription of Ball & Gizon (2014), and assuming

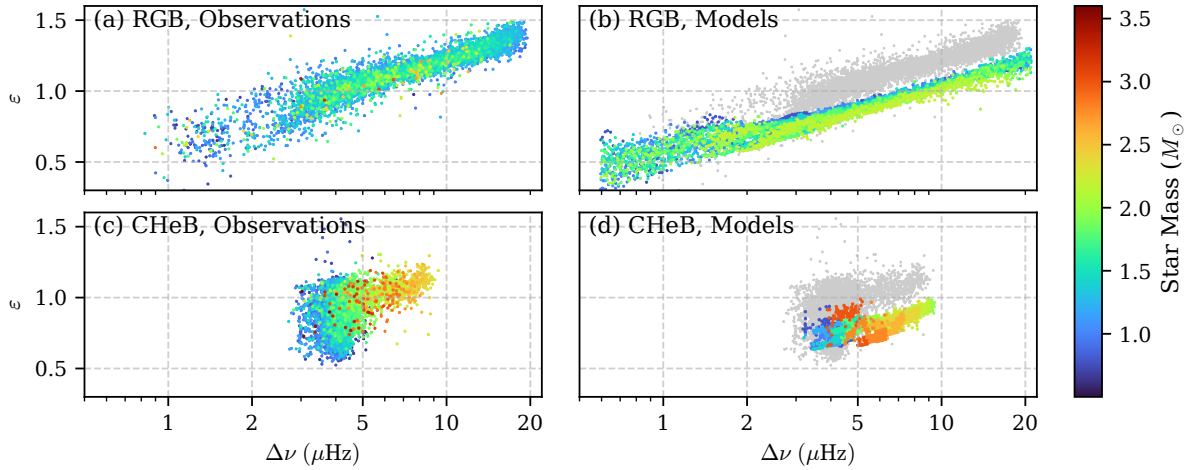

Figure 4. ε diagram, showing the comparison of observational and model results between ε and $\Delta\nu$, colour-coded by stellar mass. Panels (a)-(b) show the RGB phase, while panels (c)-(d) correspond to the CHeB phase. The grey points in the right-hand panels are the observed values.

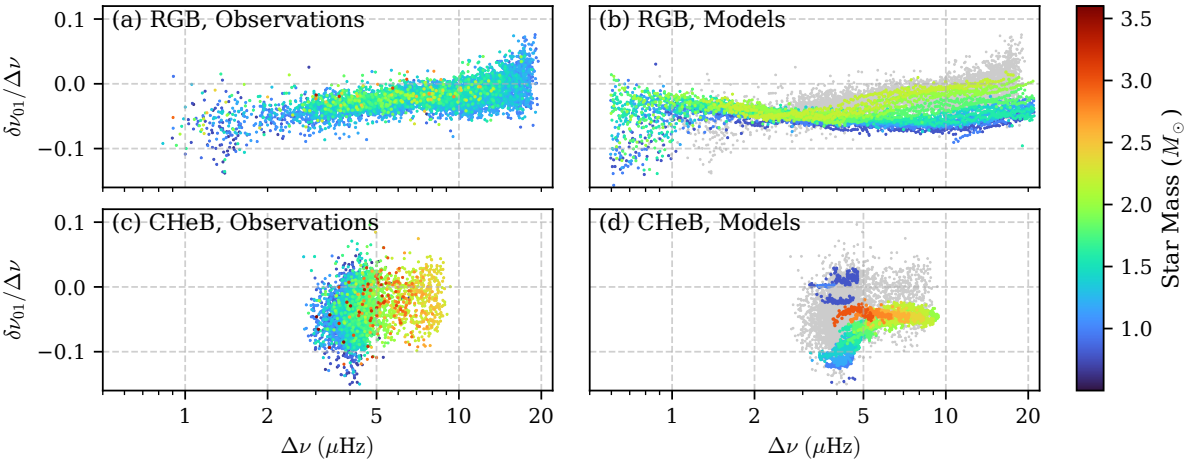

Figure 5. Same as Figure 4, but for $\delta\nu_{01}$

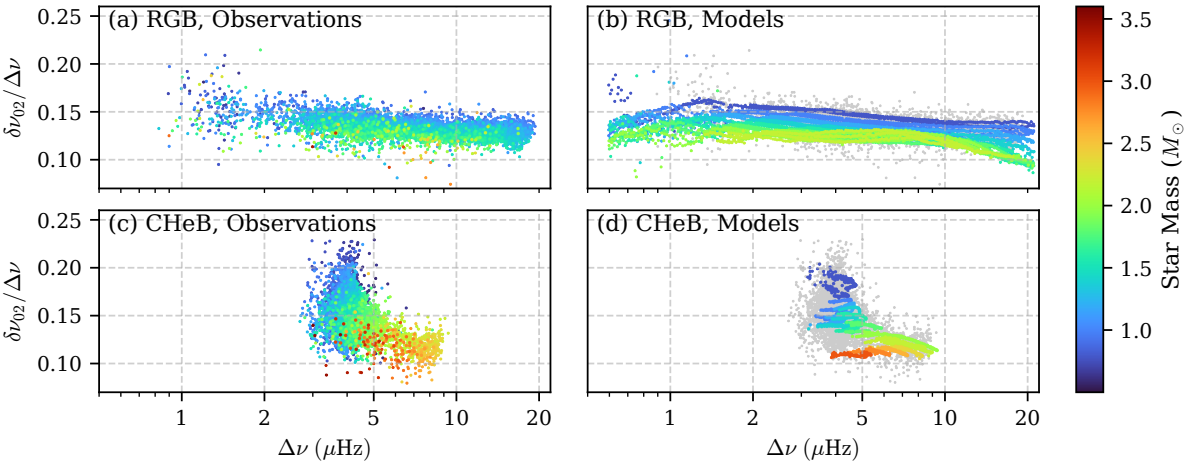

Figure 6. Ssame as Figure 4, but for $\delta\nu_{02}$

all other stellar physics were correctly modelled, such corrections should eliminate systematic offsets in both seismic diagnostics simultaneously. However, the persistent systematic offset observed in $\delta\nu_{01}$ suggests that surface effects impact $l = 1$ and $l = 0$ modes differently. This mode-dependent behaviour indicates that the $l = 1$ modes need a separate correction, rather than the uniform approach used in previous studies (e.g. Ball & Gizon 2014, 2017).

The implementation of mode-specific surface corrections could significantly improve the accuracy of stellar models for RGB stars. The consistent magnitude and direction of the offsets in $\delta\nu_{01}$ suggest that these corrections are not only necessary but also predictable, potentially allowing for systematic improvements in how stellar evolution codes model the surface.

4.3 $\delta\nu_{02}$: A Strong Constraint for Both RGB and CHeB

For RGB stars, Figure 6(a) confirms that $\delta\nu_{02}$ is proportional to $\Delta\nu$, but with a clear mass dependence. This aligns with previous studies (Huber et al. 2010; Handberg et al. 2017), which established that $\delta\nu_{02}$ remains nearly constant as a fraction of $\Delta\nu$ during the RGB stage. The observed data match theoretical predictions from the MESA and GYRE models, confirming that $\delta\nu_{02}$ can constrain stellar masses. However, its diagnostic power for RGB stars is limited, as it primarily reflects global seismic properties rather than detailed internal structure. This constancy arises because the radiative core of an RGB star evolves minimally in size, making $\delta\nu_{02}$ a stable but less informative parameter compared to $\Delta\nu$ or $\nu_{\rm max}$.

In contrast, $\delta\nu_{02}$ in CHeB stars exhibits a more complex behaviour (Figure 6(c)). A clear separation emerges, splitting stars into two distinct sequences: red clump (RC) and secondary clump (SC). This separation reflects differences in core helium ignition processes, which are mass-dependent. Low-mass RC stars undergo a helium flash at the RGB tip, creating a dense, stratified core. Higher-mass SC stars ignite helium under non-degenerate conditions, resulting in a smoother core structure (see review by Girardi 2016).

The ratio $\delta\nu_{02}/\Delta\nu$ serves as a diagnostic for these structural differences. The mass- and evolutionary-state dependence of $r_{02} \equiv \delta\nu_{02}/\Delta\nu$ was anticipated by stellar-model calculations (Montalbán et al. 2010, see their Fig. 4). An extended discussion of the underlying physics and its diagnostic use in red giants is provided by Montalbán et al. (2012). Recent TESS ensemble analysis also reports a pronounced increase of $r_{02} \equiv \delta\nu_{02}/\Delta\nu$ toward lower $\Delta\nu$, and a weaker r_{02}–$\Delta\nu$ correlation but stronger mass dependence at $\Delta\nu \gtrsim 15.6\,\mu$Hz (Zhou et al. 2025). For RC stars, the ratio spans a relatively wide range from approximately 0.12 to 0.23 in Figure 6(c), exhibiting a clear inverse correlation with stellar mass: more massive red clump stars tend to have lower values of $\delta\nu_{02}/\Delta\nu$. This trend suggests that even within the red clump, structural variations determined by mass—such as differences in core mass and envelope stratification—significantly impact the small separation.

In contrast, SC stars display a narrow distribution around $\delta\nu_{02}/\Delta\nu \sim 0.10$, with little apparent mass dependence. This mass-independent clustering is consistently reproduced by the theoretical models (Figure 6(d)), where both observations and models show little spread. The weak sensitivity of $\delta\nu_{02}/\Delta\nu$ to mass in this regime is consistent with the more gradual evolutionary transitions these stars experience: without a helium flash, the build-up of the core–envelope density contrast is smoother, so that $l = 2$ modes remain predominantly p-dominated. Consequently, $\delta\nu_{02}/\Delta\nu$ exhibits a tighter clustering near ~ 0.10 (e.g. Girardi 2016; Hekker & Christensen-Dalsgaard 2017).

Our results provides a seismic criterion to distinguish RC and SC stars. The sensitivity of $\delta\nu_{02}/\Delta\nu$ to mass in RC stars further informs calibrations of core mixing processes and convective boundary treatments (Ong et al. 2025). For SC stars, the uniformity of $\delta\nu_{02}/\Delta\nu$ suggests that helium-burning efficiency dominates over structural variations. Together, these results highlight $\delta\nu_{02}$ as a critical probe of stellar evolution, complementing $\Delta\nu$ and $\nu_{\rm max}$ in constraining internal structure.

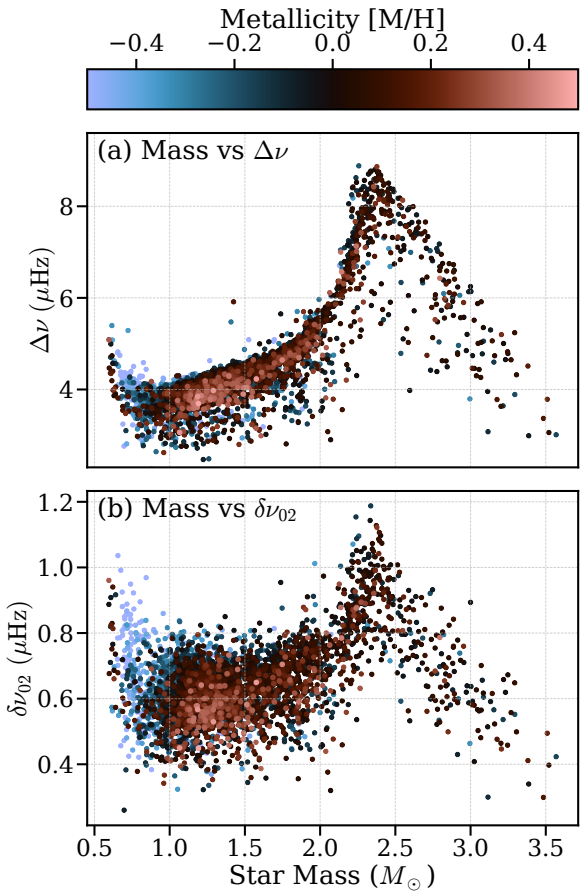

Figure 7. Core–He–burning stars with APOKASC-3 metallicities: (a) mass versus $\Delta\nu$; (b) mass versus $\delta\nu_{02}$. Points are coloured by [M/H].

4.4 Metallicity and the Helium-Flash Transition in Core He-Burning Stars

To test whether composition modulates the structure of CHeB stars, we examined the relations between stellar mass and the seismic parameters $\Delta\nu$ and $\delta\nu_{02}$ for stars classified as CHeB. These relations are shown in Figure 7, colour-coded by spectroscopic metallicity [M/H] from APOKASC-3 (Pinsonneault et al. 2025). Not all stars in our catalogue have spectroscopic metallicities; the CHeB subsample with available [M/H] contains 5063 stars.

Figure 7 reveals three qualitative features. First, in the mass-$\Delta\nu$ plane there is a sharp peak in the range 2–2.3 $M_\odot$, which corresponds to the transition between RC and SC (e.g. Girardi 1999; Girardi et al. 2000; Bressan et al. 2012; Constantino et al. 2015). Second, the mass–$\delta\nu_{02}$ relation shows a similar transition, broadly mirroring the trend in mass–$\Delta\nu$, as in Figure 6(c). Third, at fixed mass both panels display a colour gradient, suggesting that [M/H] influences either the location or the sharpness of the helium flash limit peak. This is qualitatively expected: in stellar models, the helium-flash thresh-

old mass ($M_{\rm HeF}$) depends on both composition and the treatment of convective-boundary mixing, because opacity and core growth regulate whether helium ignites under partial degeneracy.

These patterns are empirical indications rather than a calibrated relation. A quantitative test of [M/H] vs. $M_{\rm HeF}$ sensitivity would require a larger CHeB sample with spectroscopic [M/H] and uniform mass determinations, together with a grid that varies Z and envelope overshoot in a controlled way (e.g. Bossini et al. 2015; Chaplin & Miglio 2013). Future work could extend this analysis with TESS targets to increase the number of CHeB stars with [M/H], enabling a direct measurement of how metallicity shapes the observed mass–$\Delta\nu$ and mass–$\delta\nu_{02}$ sequences and the inferred helium–flash limit.

5 CONCLUSIONS

We have presented a homogeneous analysis of ∼16,000 red giants observed by *Kepler* using all available long-cadence data sets. Our work provides a comprehensive catalogue of global seismic parameters and investigates their evolutionary dependencies. The main results are summarized as follows:

(i) We provide a homogeneous catalogue of $\Delta\nu$, $\delta\nu_{01}$, $\delta\nu_{02}$, and ε for 16,050 red giants, representing the largest sample to date for these parameters. The typical (median) uncertainties are 0.3% in $\Delta\nu$, 0.0008 in $r_{01} \equiv \delta\nu_{01}/\Delta\nu$, 0.0010 in $r_{02} \equiv \delta\nu_{02}/\Delta\nu$, and 0.3% in ε.

(ii) The ratio $\delta\nu_{02}/\Delta\nu$ is nearly constant for RGB stars, consistent with theoretical models. In contrast, CHeB stars exhibit a clear separation into RC and SC sequences. This distinction reflects differences in core helium ignition processes, with $\delta\nu_{02}/\Delta\nu$ serving as a seismic diagnostic for CHeB sub-populations.

(iii) We derived a unified power-law relation $\varepsilon = 0.610 + 0.625\log_{10}(\Delta\nu)$ for all stars. Systematic offsets between observations and models indicate the effects of a poorly modelled surface (known as the "surface effect"), which are consistent across both the RGB and CHeB phases. This suggests a single surface correction prescription may apply to both types of stars.

(iv) Observed $\delta\nu_{01}$ values are systematically offset from models, with negative values for most red giants. The persistence of offsets in models after uniform surface corrections implies mode-dependent surface effects, suggesting separate corrections for $l = 1$ modes.

(v) For RC stars, $\delta\nu_{02}/\Delta\nu$ correlates inversely with mass, providing a constraint on core structure and mixing processes. SC stars show uniform $\delta\nu_{02}/\Delta\nu$ values, reflecting smoother core-envelope density contrasts. This highlights $\delta\nu_{02}$ as a critical probe of stellar evolution, complementing $\Delta\nu$ and $\nu_{\rm max}$.

These results underscore the value of small frequency separations and phase shifts in constraining stellar interiors. The $\delta\nu_{02}$ parameter, in particular, emerges as a powerful tool for distinguishing evolutionary states and probing core helium ignition processes. These measurements will allow others to leverage these parameters to refine stellar models, particularly in the treatment of surface-term corrections and convective-boundary mixing.

ACKNOWLEDGEMENTS

We acknowledge support from the Australian Research Council through Laureate Fellowship FL220100117. DH acknowledges support from the Alfred P. Sloan Foundation, the National Aeronautics and Space Administration (80NSSC19K0597 and 80NSSC21K0652) and the Australian Research Council (FT200100871).

DATA AVAILABILITY

Data Availability. The full catalogue underlying this article—containing all measured values and 1σ uncertainties for $\Delta\nu$, $\delta\nu_{01}$, $\delta\nu_{02}$ and ε—is deposited on Zenodo (reserved DOI: 10.5281/zenodo.17225960; the DOI will be registered upon publication) and will be submitted to CDS via VizieR upon acceptance. The MESA models are provided as a single Parquet file on Zenodo (reserved DOI: 10.5281/zenodo.17226468; the DOI will be registered upon publication). The *Kepler* light curves are available via the MAST Portal at https://mast.stsci.edu/portal/Mashup/Clients/Mast/Portal.html

REFERENCES

Asplund M., Grevesse N., Sauval A. J., Scott P., 2009, ARA&A, 47, 481
Baglin A., et al., 2006, in 36th COSPAR Scientific Assembly. p. 3749
Ball W. H., Gizon L., 2014, A&A, 568, A123
Ball W. H., Gizon L., 2017, A&A, 600, A128
Bedding T. R., 2012, in Shibahashi H., Takata M., Lynas-Gray A. E., eds, Astronomical Society of the Pacific Conference Series Vol. 462, Progress in Solar/Stellar Physics with Helio- and Asteroseismology. p. 195 (arXiv:1109.5768), doi:10.48550/arXiv.1109.5768
Bedding T. R., Kjeldsen H., Butler R. P., McCarthy C., Marcy G. W., O'Toole S. J., Tinney C. G., Wright J. T., 2004, ApJ, 614, 380
Bedding T. R., et al., 2010, ApJ, 713, L176
Bellinger E. P., Christensen-Dalsgaard J., 2022, MNRAS, 517, 5281
Borucki W., et al., 2008, in Sun Y.-S., Ferraz-Mello S., Zhou J.-L., eds, IAU Symposium Vol. 249, Exoplanets: Detection, Formation and Dynamics. pp 17–24, doi:10.1017/S174392130801630X
Bossini D., et al., 2015, MNRAS, 453, 2290
Bouchy F., Carrier F., 2002, A&A, 390, 205
Bressan A., Marigo P., Girardi L., Salasnich B., Dal Cero C., Rubele S., Nanni A., 2012, MNRAS, 427, 127
Chaplin W. J., Miglio A., 2013, ARA&A, 51, 353
Choi J., Dotter A., Conroy C., Cantiello M., Paxton B., Johnson B. D., 2016, ApJ, 823, 102
Christensen-Dalsgaard J., 1988, in Christensen-Dalsgaard J., Frandsen S., eds, IAU Symposium Vol. 123, Advances in Helio- and Asteroseismology. p. 295
Christensen-Dalsgaard J., 2014, in Pallé P. L., Esteban C., eds, Asteroseismology. p. 194, doi:10.48550/arXiv.1106.5946
Christensen-Dalsgaard J., Silva Aguirre V., Elsworth Y., Hekker S., 2014, MNRAS, 445, 3685
Claret A., Torres G., 2019, ApJ, 876, 134
Constantino T., Campbell S. W., Christensen-Dalsgaard J., Lattanzio J. C., Stello D., 2015, MNRAS, 452, 123
Corsaro E., et al., 2012, ApJ, 757, 190
Dhanpal S., Benomar O., Hanasoge S., Takata M., Panda S. K., Kundu A., 2023, ApJ, 958, 63
Girardi L., 1999, MNRAS, 308, 818
Girardi L., 2016, ARA&A, 54, 95
Girardi L., Bressan A., Bertelli G., Chiosi C., 2000, A&AS, 141, 371
Grec G., Fossat E., Pomerantz M. A., 1983, Sol. Phys., 82, 55
Handberg R., Brogaard K., Miglio A., Bossini D., Elsworth Y., Slumstrup D., Davies G. R., Chaplin W. J., 2017, MNRAS, 472, 979
Hekker S., Christensen-Dalsgaard J., 2017, A&ARv, 25, 1
Hon M., Stello D., García R. A., Mathur S., Sharma S., Colman I. L., Bugnet L., 2019, MNRAS, 485, 5616
Hon M., Li Y., Ong J., 2024, ApJ, 973, 154
Houdek G., Balmforth N. J., Christensen-Dalsgaard J., Gough D. O., 1999, A&A, 351, 582
Huber D., et al., 2010, ApJ, 723, 1607
Huber D., et al., 2011, ApJ, 743, 143
Jackiewicz J., 2021, Frontiers in Astronomy and Space Sciences, 7, 102
Jermyn A. S., et al., 2023, ApJS, 265, 15

Joyce M., Molnár L., Cinquegrana G., Karakas A., Tayar J., Tarczay-Nehéz D., 2024, ApJ, 971, 186
Kallinger T., 2019, arXiv e-prints, p. arXiv:1906.09428
Kallinger T., et al., 2012, A&A, 541, A51
Li Y., et al., 2023, MNRAS, 523, 916
Miglio A., et al., 2021, Astronomy & Astrophysics, 645, A85
Montalbán J., Miglio A., Noels A., Scuflaire R., Ventura P., 2010, The Astrophysical Journal Letters, 721, L182
Montalbán J., Miglio A., Noels A., Scuflaire R., Ventura P., D'Antona F., 2012, in Miglio A., Montalbán J., Noels A., eds, Astrophysics and Space Science Proceedings, Red Giants as Probes of the Structure and Evolution of the Milky Way. Springer Berlin Heidelberg, Berlin, Heidelberg, pp 23–32, doi:10.1007/978-3-642-18418-5_3
Mosser B., et al., 2010, A&A, 517, A22
Mosser B., et al., 2012, A&A, 537, A30
Mosser B., et al., 2013, A&A, 550, A126
Newville M., et al., 2025, LMFIT: Non-Linear Least-Squares Minimization and Curve-Fitting for Python, https://doi.org/10.5281/zenodo.16175987, doi:10.5281/zenodo.16175987
Ong J. M. J., Basu S., 2019, ApJ, 885, 26
Ong J. M. J., Basu S., 2020, ApJ, 898, 127
Ong J. M. J., Lindsay C. J., Reyes C., Stello D., Roxburgh I. W., 2025, ApJ, 980, 199
Otí Floranes H., Christensen-Dalsgaard J., Thompson M. J., 2005, MNRAS, 356, 671
Paxton B., Bildsten L., Dotter A., Herwig F., Lesaffre P., Timmes F., 2011, ApJS, 192, 3
Paxton B., et al., 2013, ApJS, 208, 4
Paxton B., et al., 2015, ApJS, 220, 15
Paxton B., et al., 2018, ApJS, 234, 34
Paxton B., et al., 2019, ApJS, 243, 10
Pinsonneault M. H., et al., 2025, ApJS, 276, 69
Planck Collaboration et al., 2016, A&A, 594, A13
Reyes C., Stello D., Ong J., Lindsay C., Hon M., Bedding T. R., 2025, Nature, 640, 338
Ricker G. R., et al., 2015, Journal of Astronomical Telescopes, Instruments, and Systems, 1, 014003
Roxburgh I. W., 2005, A&A, 434, 665
Roxburgh I. W., Vorontsov S. V., 2003, A&A, 411, 215
Samadi R., Goupil M. J., 2001, A&A, 370, 136
Smith J. C., et al., 2012, PASP, 124, 1000
Sreenivas K. R., Bedding T. R., Li Y., Huber D., Crawford C. L., Stello D., Yu J., 2024, MNRAS, 530, 3477
Stello D., Cantiello M., Fuller J., Garcia R. A., Huber D., 2016a, Publ. Astron. Soc. Australia, 33, e011
Stello D., Cantiello M., Fuller J., Huber D., García R. A., Bedding T. R., Bildsten L., Silva Aguirre V., 2016b, Nature, 529, 364
Stumpe M. C., et al., 2012, PASP, 124, 985
Tassoul M., 1980, ApJS, 43, 469
Townsend R. H. D., Teitler S. A., 2013, MNRAS, 435, 3406
Vrard M., et al., 2015, A&A, 579, A84
Vrard M., et al., 2025, A&A, 697, A165
White T. R., Bedding T. R., Stello D., Christensen-Dalsgaard J., Huber D., Kjeldsen H., 2011, ApJ, 743, 161
Yu J., Huber D., Bedding T. R., Stello D., Hon M., Murphy S. J., Khanna S., 2018, ApJS, 236, 42
Zhou J., et al., 2025, The Astrophysical Journal Supplement Series, 279, 37
Zinn J. C., Stello D., Huber D., Sharma S., 2019, ApJ, 884, 107

This paper has been typeset from a TEX/LATEX file prepared by the author.